Adaptive optical coherence-domain reflectometry using photorefractive quantum wells

Leilei Peng and David D. Nolte

Department of Physics, Purdue University, West Lafayette, Indiana 47907-1396

Ping Yu

Department of Physics and Astronomy, University of Missouri-Columbia, Columbia, Missouri 65211

Michael R. Melloch

School of Electrical and Computer Engineering, Purdue University, West Lafayette, Indiana 47907

Received March 7, 2004; revised manuscript received June 4, 2004

Adaptive optical-coherence-domain reflectometry (OCDR) is performed by use of an adaptive interferometer and homodyne detection. The adaptive element of the interferometer is a photorefractive quantum-well device in a two-wave mixing geometry. The mixing self-adaptively maintains constant relative phase between the signal and reference waves and dynamically compensates gross movements of the sample or optical components as well as image speckle. The application described here is used for laser ranging into and through turbid media. Adaptive OCDR is a bridge between conventional optical coherence tomography and adaptive holographic optical coherence imaging. The insertion loss for the adaptive performance is −15 dB, but adaptive OCDR has potential applications for coherence tomography under conditions of large target motion and low background. We also demonstrate its potential application for optoacoustics and laser-based ultrasound detection.

OCIS codes: 090.2880, 160.5320, 190.7070.

1. INTRODUCTION

Optical coherence-domain reflectometry (OCDR) is a high-resolution laser-ranging technique that emerged at the end of 1980s.[1,2] It is based on reflectometry with low-coherence light, which coherently gates reflections by matching their optical path length with a reference. It was later developed into optical coherence tomography[3] (OCT), which combines OCDR and scanning in at least one lateral dimension for noninvasive imaging of biological tissue.

OCT systems typically use rapid-scan heterodyne detection for signal demodulation with repetitive signal averaging. Significant sample motion or environmental vibration can lead to motional artifacts in the signal demodulation and the reconstructed images. For this reason, OCT is usually restricted to the so-called B-scan. There have been increasing developments in *en face* (transverse scanning) OCT using external phase-modulation heterodyne detection, but the technique is still subject to motional artifacts.[4] Adaptive interferometry could prevent motion artifacts in signal demodulation and might facilitate the use of less-common nonscanning OCT applications, such as *en face* acquisition performed at a fixed reference delay.

Another advantage of adaptive holographic interferometry in OCT applications is automatic speckle reduction. In OCT, the goal of speckle reduction is to suppress high-spatial-frequency speckle generated by wide-angle multiple scattering, while preserving image-bearing speckle that arises from single backscattering or small-angle forward scattering. Different speckle-reduction methods have been discussed in the literature,[5] although no general method has yet been developed. Adaptive holography adapts to speckle sizes that are larger than the hologram fringe spacing. Therefore it can extract information from speckle selectively by speckle size and is free of speckle artifacts because of its wave-front-matching ability. The cut-off speckle size can be adjusted by changing the fringe spacing. Thus the system may also be versatile for detecting structures on different scales. In addition, time-varying speckle can be compensated in adaptive holography. This gives adaptive interferometry the possibility of detecting structure beneath or inside dynamic media. One approach using adaptive interferometry is holographic optical coherent imaging[6] to acquire real-time fly-though movies of biological tissue, which is different from point-by-point scanning in OCT.

In this paper, adaptive OCDR using a photorefractive quantum-well[7] (PRQW) device is explored. Adaptive OCDR inherits the same point-scan detection mode from conventional OCDR and differs only in that an adaptive component is used to mix the signal with the reference field. The principle of adaptive OCDR has also been demonstrated previously using an adaptive photoelectromotive-force detector,[8,9] yet the microwatt-level sensitivity of this method is not enough for biological imaging. A more practical method is based on high-speed adaptive homodyne interferometry.[10–13]

0740-3224/2004/111953-11$15.00

This paper describes the physics and performance of adaptive OCDR in the case when the mixer is a photorefractive quantum-well device, and the adaptive beam combination is performed through two-wave mixing.[14] Section 2 describes the system setup. Two-wave mixing with a broadband source is separated into the processes of hologram recording, hologram readout, and homodyne detection in Sections 3, 4, and 5, respectively. Section 6 discusses the sensitivity of adaptive OCDR in comparison with OCT and holographic optical coherent imaging. Section 7 describes the application to ultrasound detection inside a turbid medium.

2. SYSTEM SETUP

A schematic diagram of an adaptive homodyne interferometer is shown in Fig. 1. It is divided into three conceptual components: the source, the mixer, and the detector. Each of the elements has an independent spectral response centered on independent central frequencies. The source generating the signal and reference waves has a broadband amplitude spectrum S with a width of $\Delta\omega_s$ centered at ω_s. The reference phase is modulated sinusoidally at high frequency to generate a homodyne signal at the detector. The signal and reference furthermore have a relative delay τ. The mixer combines the signal and reference with a complex transfer function q centered at ω_q with a bandwidth $\Delta\omega_q$, whose square Q is shown in Fig. 1. The detector consists of a spectrometer in front of a photodetector. The spectrometer power-transfer function D is centered at ω_d with a spectral width $\Delta\omega_d$. Each center frequency and bandwidth contributes to the detected signal that varies as a function of the delay τ.

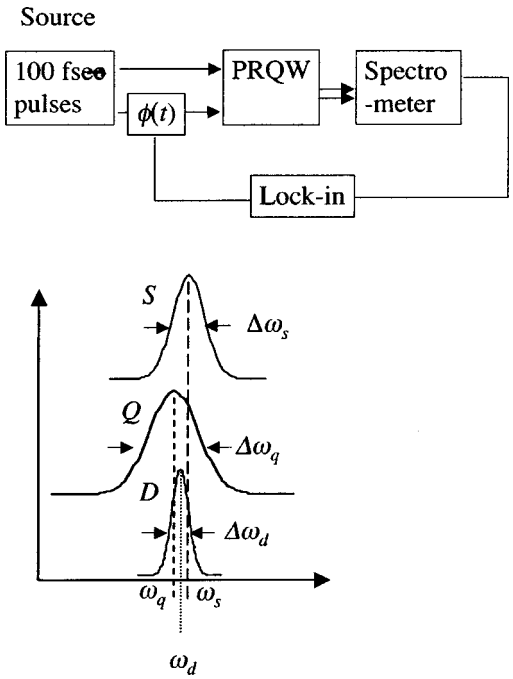

Fig. 1. Schematic drawing of adaptive homodyne interferometry. Signal and reference fields from the same source $S(\omega - \omega_s)$ are mixed by a PRQW device with a complex transfer function of $Q(\omega - \omega_q)$. The reference is phase modulated by $\phi(t)$, and by being reflected back from a sample, the signal has a delay τ in time. Homodyne signals from the mixed fields are detected through a spectrometer with a transfer function of $D(\omega - \omega_d)$. A lock-in amplifier is used to readout the homodyne signal with $\phi(t)$ as synchronization.

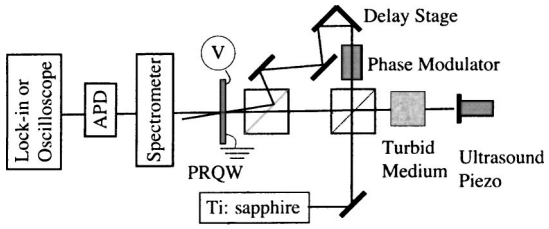

Fig. 2. Adaptive OCDR experimental setup.

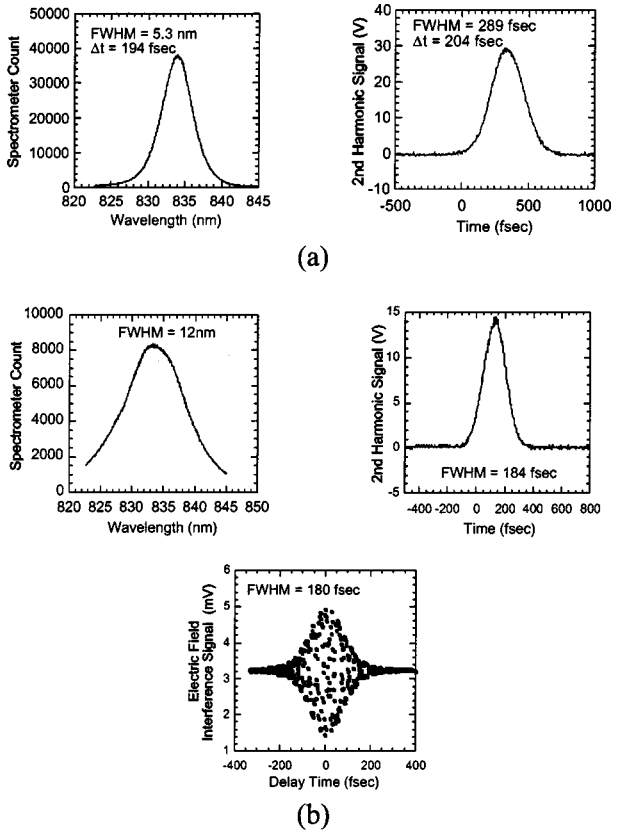

Fig. 3. Pulse-characterization results: (a) Spectrum and second-harmonic intensity autocorrelation of 5-nm-bandwidth nominal pulses. (b) Spectrum, second-harmonic intensity autocorrelation, and electric field autocorrelation of 12-nm-bandwidth pulses. The electric field correlation function gives a FWHM of 180 fs, corresponding to a 27-μm depth resolution in reflectometry.

Figure 2 is the experimental setup of the adaptive OCDR system. The source is a 100-MHz self-mode-locked Ti:sapphire laser (Clark-MXR, NJA-1) that generates nominal 200-fs broadband pulses. Figure 3(a) shows the pulse spectrum and second-harmonic intensity autocorrelation trace. The relative delay τ path length is controlled on the reference arm by a 0.1-μm-resolution stepping-motor delay stage (Newport, UE72PP). The target in this study was a mirror at the end of the signal arm. Phase modulation $\phi(t)$ comes from two alternative sources: a resonant phase modulator (Newfocus, 4001) in the reference beam working at 5 MHz with an optimal

$\Delta_\phi = \pi/3$, or an ultrasound piezo (Panametrics, A303R) that is attached to the target mirror, providing a pulsed surface vibration with a 2-MHz center frequency (for ultrasound experiments). To test the system sensitivity, a 1-cm-cubic cuvette filled with a water solution of 1-μm-diameter polystyrene beads (Bangs Laboratories, PS04N) was placed in the reflection path. The optical thicknesses of the turbid media were calculated by Mie theory and calibrated using the laser and a powermeter.

3. HOLOGRAM RECORDING WITH A BROADBAND SOURCE

When a hologram is written by a broadband source with a repetition rate much higher than the hologram response time, the holographic grating is in a steady-state condition, responding as if the source were cw rather than pulsed. Furthermore, if the bandwidth of the source is much smaller than the central frequency, then there is no reduction in the hologram contrast relative to a narrowband cw laser. For this reason, the holographic grating in a photorefractive material is not sensitive to the properties of the source, as long as there is zero path difference between the reference and signal waves. In this case, in response to a sinusoidal interference pattern, a photorefractive quantum-well structure records a hologram as a spatial modulation in the optical refractive index.

Assuming the signal beam is a single reflection from the target without any incoherent background, when a delay (or a difference in the optical path length) does exist between the signal and the reference, the fields are

$$E_s(\omega) = \sqrt{I_s}s(\omega - \omega_s)\exp(i\omega\tau),$$
$$E_r(\omega) = \sqrt{I_r}s(\omega - \omega_s), \tag{1}$$

where $I_s I_r$ are the signal and reference intensities, respectively, $s(\omega - \omega_s)$ is the spectral amplitude of the light source, and the signal is delayed relative to the reference by the time τ. In this case, the gratings are still static, but their amplitude and phase depend on the delay τ. The index grating is described by[14]

$$\tilde{n}(x, \omega_s) = \tilde{n}(\omega_s) + \delta\tilde{n}(\omega_s)m(\tau)\cos(Kx + \phi_P + \omega_s\tau), \tag{2}$$

where $m(\tau)$ is the delay-dependent modulation function, which is the time-domain convolution of the signal and reference fields and can be calculated from Eq. (1), $\tilde{n}(\omega)$ is the average complex refractive index under the applied electric field, and $\delta\tilde{n}(\omega_s)$ is the optical frequency-dependent complex amplitude of the hologram. The spatial grating $m(\tau)\cos(Kx + \phi_P + \omega_s\tau)$ considers only the lowest spatial harmonic with spatial frequency K that gives the strongest diffraction, and also includes the phase shift caused by the relative delay as well as the contrast. The phase ϕ_P is the photorefractive phase shift that represents the phase offset between the intensity pattern and the optical index pattern driven by the space-charge formation.[15,16] The refractive index $\tilde{n}(\omega)$ and $\delta\tilde{n}(\omega)$ are

$$\tilde{n}(\omega) = n(\omega) + i\frac{\alpha(\omega)}{2k}, \quad \delta\tilde{n}(\omega) = \delta n(\omega) + i\frac{\delta\alpha(\omega)}{2k}, \tag{3}$$

where $\alpha(\omega)$ is the absorption coefficient.

A. Depth Resolution of Adaptive OCDR

As shown in Eq. (2), depth resolution of the system is decided by the modulation function $m(\tau)$. For a relative time delay τ between the signal and reference waves, the modulation function $m(\tau)$ acquires a spatial dependence that is a function of τ as well as the coherence time t_c of the source. Conventional OCDR uses electric field cross correlation between signal and reference pulses as the means to provide the coherence-gated depth resolution. The full width at half-maximum (FWHM) of the electric field cross correlation for the reflected signal of a transform-limited Gaussian pulse is given by $\Delta d = ct_p$, where t_p is the pulse duration. In the case of adaptive OCDR, holographic two-wave mixing is also an effect of two electric fields interfering, and the adaptive approach nominally gives the same resolution as electric field cross correlation. However, because the hologram requires off-axis beams instead of a copropagating beam arrangement, the resolution is influenced by the different arrangement. A detailed study of holographic electric field cross correlation of symmetric off-axis four-wave mixing (where the signal and reference beams are both off axis) in PRQW devices was performed in Ref. 17. Following the same procedure, we here consider the case for two-wave mixing.

In symmetric off-axis holographic beam mixing, the two beams are tilted symmetrically from the PRQW device normal direction by an angle of θ. Owing to the off-axis beam arrangement, the relative delay time between the two beams changes linearly across the PRQW device window. For a certain delay τ, the path-matched position will be shifted away from the center by

$$x_0(\tau) = \frac{c\tau}{2\sin(\theta)}. \tag{4}$$

Thus the modulation index m is a function of both delay time τ and position x. The homodyne signal generated by a PRQW device with a window aperture width of W depends linearly on the integral of the modulation index across the window,

$$|\delta I_d(\omega, \tau)| \propto \frac{1}{W}\int_{-W/2}^{W/2} m(x, \tau)\mathrm{d}x. \tag{5}$$

For transform-limited Gauss pulses, relation (5) yields

$$|\delta I_d(\omega, \tau)| \propto \mathrm{erf}\left\{\frac{[4\ln(2)]^{1/2}[W/2 + x_0(\tau)]}{\Delta x}\right\} + \mathrm{erf}\left\{\frac{[4\ln(2)]^{1/2}[W/2 - x_0(\tau)]}{\Delta x}\right\}, \tag{6}$$

here Δx is the FWHM of the modulation function $m(\tau, x)$ across the PRQW device window and is given by $\Delta x = ct_p/\sin(\theta)$. Relation (6) can be evaluated numerically. At the limit of large t_p or small window aperture W, relation (6) gives adaptive OCDR the same depth resolution as conventional OCDR. In the small t_p limit, the integral over the window gives a depth resolution larger than the direct electric field correlation and introduces the minimal distinguishable pulse duration. The depth resolution of adaptive OCDR cannot be improved beyond the minimum distinguishable pulse duration. Figure 4 shows numerical results based on relation (6) for $\theta = 0.01$ rad (equivalent to 40-μm fringe space at 830-nm center wavelength) with different window sizes, as well as the depth resolution of electric field correlation calculated by $\Delta d = ct_p$. The separation between the two curves decreases with increasing pulse duration, whereas for a 1-mm-wide window, when the pulse duration is smaller than the 15 fs (the minimal distinguishable duration), adaptive OCDR depth resolution remains at 10 μm. As shown in Fig. 4, decreasing W can improve the minimum distinguishable pulse duration and improve the depth resolution.

Relation (6) is not valid when the pulse is not transform limited, but the principle of minimum distinguishable pulse duration can be extended to a principle of maximal distinguishable spectrum bandwidth. With a non-transform-limited pulse, the modulation index function is

$$m(x, \tau) = \frac{2\sqrt{I_s I_r}}{I_s + I_r}\Gamma[\tau - 2x\sin(\theta)/c], \tag{7}$$

where $\Gamma(\tau)$ is the electric field autocorrelation function of the pulse, which is the Fourier transform of the power spectrum $P(\omega)$. The FWHM of the electric field autocorrelation $\Delta\tau$ is set by the width of the power spectrum $\Delta\omega$,

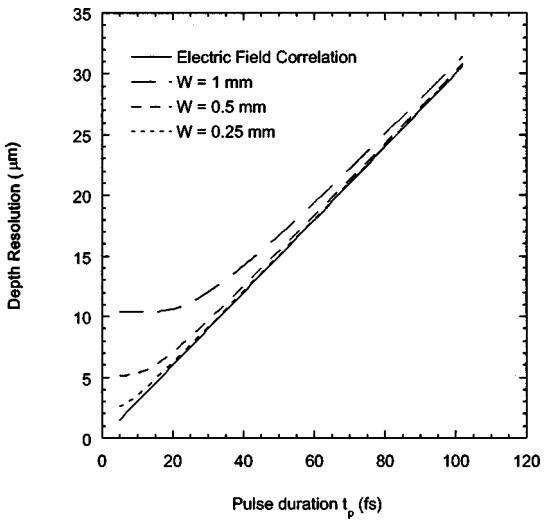

Fig. 4. Depth resolution of adaptive OCDR (solid curve) and conventional OCDR (dashed curve) for $\theta = 0.01$ rad and $W = 1$, 0.5, 0.25 mm. The minimum distinguishable pulse duration in this case is 20 fs for the 1-mm window. The lower limit of adaptive OCDR depth resolution is 10 μm for the 1-mm window.

$$\Delta\tau = \xi\frac{1}{\Delta\omega}, \tag{8}$$

where ξ is a constant decided by the shape of the power spectrum [equal to $4\ln(2)/\pi$ for a Gaussian spectrum]. The FWHM of the modulation function across the PRQW device window will be

$$\Delta x = \frac{c\Delta\tau}{2\sin(\theta)} = \frac{c}{2\sin(\theta)}\xi\frac{1}{\Delta\omega}. \tag{9}$$

When the bandwidth of the spectrum is large enough to make Δx comparable with the width of the PRQW device window, the integration across the window makes the depth resolution of the homodyne signal depend more on the window size than the autocorrelation time width, and using a wider spectrum will not improve the depth resolution. In the case of transform-limited pulses, 15-fs pulses with a spectrum centered at 830 nm with 7-nm bandwidth gives a Δx equal to half of the 1-mm window for $\theta = 0.01$ rad. Thus in this geometry, the maximum distinguishable bandwidth is 7 nm.

B. Reference Phase Modulation

For homodyne detection with a large phase modulation $\phi(t)$ in the reference arm, the rapidly modulated phase moves the hologram fringes at a speed higher than the response rate of the photorefractive quantum-well material (kilohertz in the dark to megahertz for laser intensities of approximately 100 mW/cm^2).[15] The photorefractive quantum-well device records the time average of the shifting hologram, producing an effective modulation index $\langle m\rangle$ that takes the place of the original modulation index m. For a sinusoidal phase modulation given by

$$\phi(t) = \Delta_\phi\sin(\Omega t), \tag{10}$$

where Ω is a phase-modulation frequency greater than the response rate of the photorefractive quantum-wells device, the effective modulation is

$$\langle m\rangle = m(\tau)\frac{\Omega}{\pi}\int_0^{\pi/\Omega}\cos[\Delta_\phi\sin(\Omega t)]\mathrm{d}t = m(\tau)J_0(\Delta_\phi), \tag{11}$$

where J_0 is a Bessel function. Owing to the fringe washout, $\langle m\rangle$ decreases as the phase-modulation amplitude increases. Figure 5(a) shows the simulated $\langle m\rangle$ as a function of the phase-modulation amplitude based on Eq. (11). The amplitude of the homodyne signal δP_d as a function of Δ_ϕ is a trade-off between strong phase modulation and effective modulation index loss,

$$\delta P_d(t) \propto \sin(\Delta_\phi)J_0(\Delta_\phi). \tag{12}$$

Relation (12) gives a maximum homodyne signal when $\Delta_\phi \approx \pi/3$. Figure 5(b) is the experimental plot of the homodyne signal with increasing phase modulation, compared with the theoretical curve from relation (12).

4. BROADBAND HOLOGRAM READOUT

In contrast to the writing process, the hologram readout is strongly dependent on the broadband spectrum of the readout pulse and the relative central frequencies ω_s and

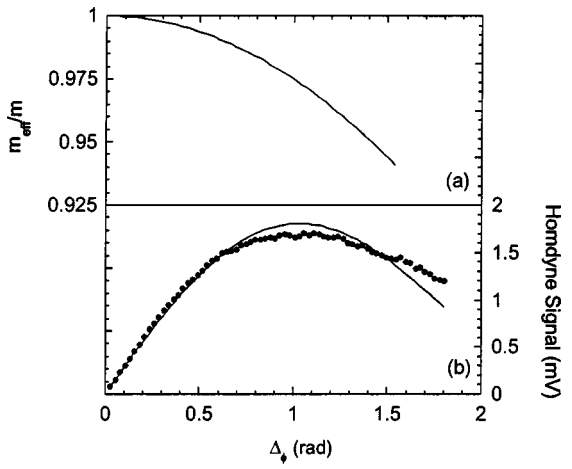

Fig. 5. (a) Effective modulation index $\langle m \rangle$ versus phase-modulation amplitude. (b) Homodyne signal versus phase-modulation amplitude, experiment results (data points), and theoretical curve (solid curve). Both show a maximum at $\Delta_\phi \approx \pi/3$.

ω. We consider only the case of degenerate four-wave mixing for which the central frequency of the writing and readout pulses are the same. Indeed, the reference pulse is the readout pulse in this case.

After transmission through a photorefractive quantum-well device with a thickness L under a transverse field, the zero-order transmission of the signal and the first-order diffraction of the reference copropagate toward the detector. Each is acted on by the transfer function of the PRQW. An important component of the photorefractive quantum-well device transfer function is the two-wave coupling coefficient,

$$\gamma(\omega - \omega_q) = \delta n(\omega) kL/\cos(\theta) + i\,\delta\alpha(\omega) L/2\cos(\theta) = 2\sqrt{\eta(\omega - \omega_q)}\exp[i\psi(\omega)], \tag{13}$$

where $\eta(\omega - \omega_q)$ is the diffraction efficiency centered at ω_q, and $\psi(\omega)$ is called the excitonic spectral phase,[16]

$$\psi(\omega) = \tan^{-1}\left[\frac{\delta\alpha(\omega)}{2\,\delta n(\omega) k}\right], \tag{14}$$

for which $\mathrm{d}\psi/\mathrm{d}\omega = T_2$, where T_2 is the excitonic free-induction decay time.

The zero- and first-order diffraction transfer functions are

$$q_0(\omega) = \exp[in(\omega)kL/\cos(\theta)]\exp[-\alpha(\omega)L/2]$$
$$q_1(\omega - \omega_q) = q_1'(\omega - \omega_q)\exp\{i[\psi(\omega) + \phi_P + \pi/2 + \omega_s\tau]\}, \tag{15}$$

where the zero-order transfer is absorption and delay function, and the first-order diffraction transfer, which is generated by the index grating described in Eq. (2), has an amplitude written as

$$q_1'(\omega - \omega_q) = q_0(\omega)\langle m(\tau)\rangle\sqrt{\eta(\omega - \omega_q)}. \tag{16}$$

We have retained the explicit phase of the diffraction transfer separately from the amplitude $q_1'(\omega)$. The phase of the first-order diffraction contributions are important for the homodyne detection process described in Section 5. The zero- and first-order fields are now

$$E_s(\omega, L) = q_0(\omega)\sqrt{I_s}s(\omega - \omega_s)\exp(i\omega\tau),$$
$$E_r(\omega, L) = q_1'(\omega - \omega_q)\sqrt{I_r}s(\omega - \omega_s) \times \exp\{i[\psi(\omega) + \phi_P + \pi/2 + \omega_s\tau]\}, \tag{17}$$

and the mixed electric field of the transmitted signal beam and first-order diffraction of the reference beam is

$$E_d(\omega) = q_0(\omega)\sqrt{I_s}s(\omega - \omega_s)\exp(i\omega\tau) + q_1'(\omega - \omega_q)\sqrt{I_r}s(\omega - \omega_s) \times \exp\{i[\psi(\omega) + \phi_P + \pi/2 + i\omega_s\tau]\}. \tag{18}$$

The diffracted power is finally

$$P_d(\omega) = I_s Q_0(\omega) S(\omega - \omega_s) + Q_0'(\omega - \omega_0)\sqrt{I_r I_s}S(\omega - \omega_s)\cos[\psi(\omega) + \phi_P + \pi/2 - (\omega - \omega_s)\tau], \tag{19}$$

where

$$Q_0(\omega) = |q_0(\omega)|^2,$$
$$Q_0'(\omega - \omega_0) = 2|q_1'(\omega - \omega_q)||q_0(\omega)|,$$

and

$$S(\omega - \omega_s) = |s(\omega - \omega_s)|^2.$$

It is important to note that there are two different spectral responses in the mixing term of Eq. (19), $Q_0'(\omega - \omega_q)$ and $S(\omega - \omega_s)$ for the PRQW device and the source, respectively, centered at different center frequencies ω_q and ω_s. This dual dependence produces rich frequency dependence during the homodyne detection, discussed in the next section.

5. HOMODYNE DETECTION

Under the phase modulation $\phi(t)$ of Eq. (10), the homodyne power detected at optical angular frequency ω and modulation angular frequency Ω is

$$P_\Omega(\omega;\, \omega_s,\, \omega_q) = 2\sqrt{I_r I_s}|q_1'(\omega - \omega_q)||q_0(\omega)|S(\omega - \omega_s) \times \sin[\psi(\omega) + \phi_P - (\omega - \omega_s)\tau + \Delta_\phi\cos\Omega t]. \tag{20}$$

This power is detected through a spectrometer with a power transfer function $D(\omega - \omega_d)$ with an adjustable bandwidth $\Delta\omega_d$ and center frequency ω_d. The filtered homodyne power is therefore

$$P_\Omega = \int_0^\infty P_\Omega(\omega;\, \omega_s,\, \omega_q) D(\omega - \omega_d)\mathrm{d}\omega. \tag{21}$$

In our experiments, this power is measured at two extremes for the detection bandwidth: narrow-band detection with $\Delta\omega_d \ll \Delta\omega_s,\ \Delta\omega_q$, and broadband detection with $\Delta\omega_d \gg \Delta\omega_s,\ \Delta\omega_q$. These cases are discussed in Subsections 5.A and 5.B, respectively.

We performed three types of experiments that used the broadband light source. At first, to study the detail of the homodyne spectra, adaptive laser ranging with narrow-band detection was performed with an ideal-

phase modulation from the phase modulator. The homodyne signal was detected by an avalanche photodiode (APD) (Hamamatsu, C5460) with a spectrometer placed in front of the detector (Fig. 2). Electric signals from the detector were read out by a RF lock-in amplifier that was synchronized with the phase modulation at 5 MHz. The second experiment tested the sensitivity of this technique for penetrating turbid media, in which broadband detection was used by removing the spectrometer. The third experiment was ultrasound detection combined with laser ranging. In this experiment, the phase modulator was turned off, and the ultrasound piezomirror was used to simulate ultrasound at a surface buried beneath the turbid medium. The temporal responses of the homodyne signals were detected using a digital oscilloscope in an averaged acquisition mode.

A. Narrow-Band Detection

Conventional OCDR extracts information by a pure time-domain process, i.e., correlating signal and reference electric field in the time domain. Our approach to adaptive OCDR combines both time- and spectral-domain processes. The hologram is written by time-domain interference, while two-wave mixing generates spectral interference between the signal and reference. As described above, the spectral interference in adaptive OCDR plays a unique role in adaptive laser ranging, and makes the signal trace sensitive to both the light-source spectrum as well as the optical frequency range that is detected.

The narrow-band detected power from Eq. (21) is

$$P_\Omega = 2\sqrt{I_r I_s}|q_1'(\omega_d - \omega_q)||q_0(\omega_d)|S(\omega_d - \omega_s)\sin[\psi(\omega_d) + \phi_P - (\omega_d - \omega_s)\tau + \Delta_\phi \cos \Omega t]\Delta\omega_d, \quad (22)$$

where the detector bandwidth $\Delta\omega_d$ is assumed small relative to all other bandwidths. In Eq. (22), the delay-dependent linear factor $q_1'(\omega_d - \omega_q)$ [defined in Eq. (16)] gives the homodyne-power delay dependence with the maximum at τ equal to zero. Two important special cases in terms of the optical frequency ω_d are identified in Eq. (22), when the total phase

$$\psi(\omega_d) + \phi_P = \begin{cases} 0, \pi \\ \pm\pi/2. \end{cases} \quad (23)$$

In the first case, at τ equal to zero, the homodyne power depends linearly on Δ_ϕ, which is the condition of "quadrature," when the diffracted reference and transmitted signal waves have an optimal relative phase of $\pi/2$. The second case is when the homodyne power goes to zero. It is also important to note that there are two quadratures that respond with opposite sign to Δ_ϕ.

Figure 6(a) shows narrow-band adaptive homodyne signals from a single reflection as a function of the reference delay time. The laser spectrum was centered at 834 nm with a 5-nm bandwidth. With a spectrometer in front of the photodetector, homodyne signals were detected at several wavelengths with a 0.5-nm bandwidth. These traces show oscillation in the homodyne signals as a function of delay time with decreasing oscillation period as the detecting wavelength shifted away from the center wavelength. These oscillations represent the spectral phase difference between first-order diffraction pulse and the transmission pulse, which is mainly, but not exclusively, the phase-dispersion component $(\omega_d - \omega_s)\tau$ that comes from the phase velocity of difference frequency and generates the delay-dependent oscillation with its period inversely proportional to the difference between the central detection frequency and the central source frequency. In addition, any irregular spectral phase such as chirp in the pulse will distort these oscillations. Thus adaptive homodyne can provide additional phase information on the reflection pulse, whereas electric field correlation in conventional OCDR cannot. Figure 6(b) shows the simulation results corresponding roughly to the condition of Fig. 6(a) that is numerically calculated based on Eq. (22). There are similar oscillation trends in the numerical simulation. But because simulation is based on the assumption of transform-limited pulses, the result is symmetric for negative and positive delay time in Fig. 6(b). The asymmetry of the experiment data in Fig. 6(a) is probably caused by pulse chirp from the laser source.

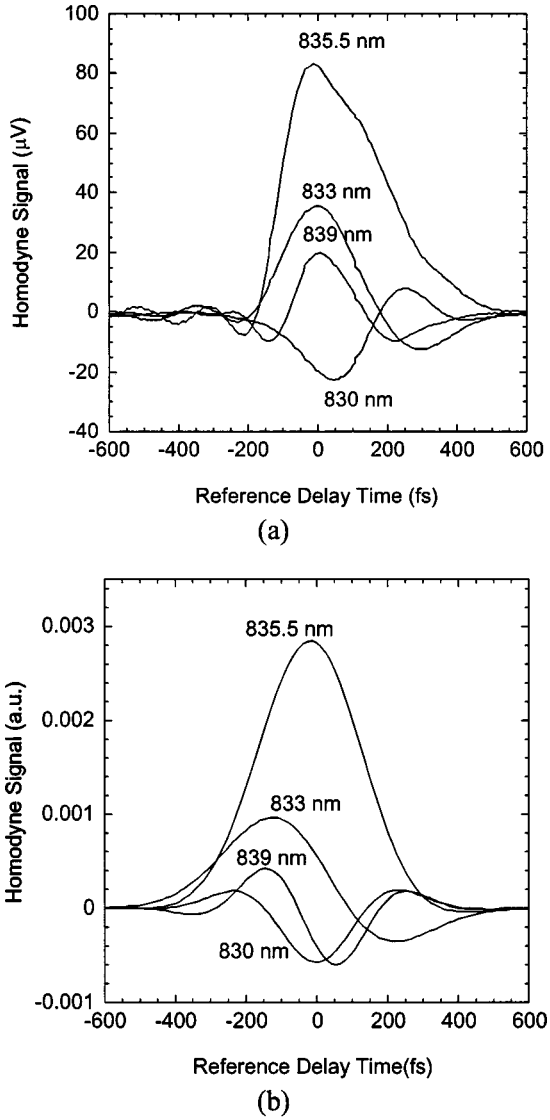

Fig. 6. Adaptive OCDR delay-line traces by narrow-band homodyne detection. The wavelengths are the detection wavelengths. (a) Experiment results with 0.5-nm detection bandwidth. (b) Simulation results under the same experimental conditions.

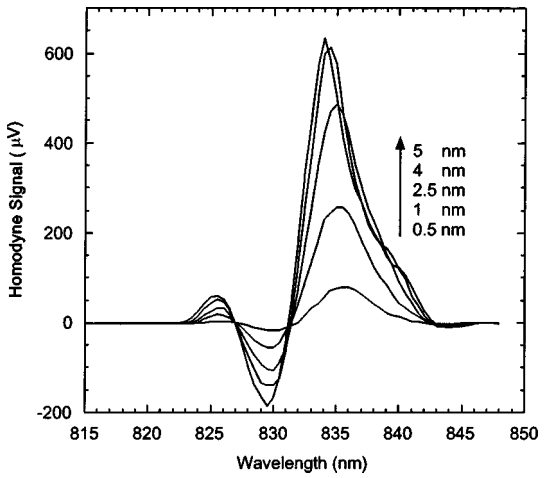

Fig. 7. Homodyne signal with increasing detection bandwidth. The homodyne signals with broadband pulses were detected at 0.5-, 1-, 2.5-, 4-, and 5-nm detection bandwidths.

B. Broadband Detection

When the spectrometer is removed, the full bandwidth of the homodyne signal is collected by the photodetector. Without any loss in the spectrometer, this broadband detection has higher photon flux than the narrow-band detection. Figure 7 shows the homodyne signal wavelength scan with broadening detection bandwidths. The signal increases significantly with larger detection bandwidth.

Because of the phase dispersion, changes in the input pulse spectrum cause significant changes in the shape of the broadband signal traces. Figure 8(a) plots the broadband detected signal with 5-nm-bandwidth laser pulses. The experimental trace shows a single positive peak, whereas simulation results in Fig. 8(b) produce a dominant positive peak with a small negative valley on the tail. After we expanded the pulse bandwidth to 12 nm, the experimental homodyne trace showed similar but weaker oscillatory behavior, as in the narrow-band-detected trace. A negative peak grew on the left tail of Fig. 9(a), while in the simulation result [Fig. 9(b)], the negative lobe is more dramatic. The peak width of the simulation is narrower than experiment because the simulation always assumes transform-limited pulses, which cannot be produced by our self-mode-locked Ti:sapphire laser with such wide bandwidth. The negative lobe is the effect of the frequency–time phase integrated over the full spectrum, and is pronounced only when the spectrum is wide enough that the phase contribution from the wings of the spectrum is large enough to overcome the central part of the spectrum at delay times that are far from zero.

From the point of view of spectral interferometry,[18] these effects of phase dispersion represent the spectral interference between a pulse (zero order of the signal) and the same pulse (first-order diffraction of the reference) that is phase shifted by $\omega_s\tau + \phi_P + \pi/2$ and delayed by T_2, which are put together by a PRQW device as an adaptive pulse mixer.[19]

6. SENSITIVITY AND DYNAMIC RANGE

The adaptive performance comes with a cost that may reduce its sensitivity (minimal detectable reflection power) relative to conventional OCDR. In the large-signal limit, the signal-to-noise ratio (SNR) of the adaptive system is limited by the Joule heating of the PRQW device, which limits the maximum light intensity the device can support. Consequently, the reference-beam intensity cannot be large when the signal beam is strong. On the other hand, in the small-signal limit, the system is limited by electronic noise of the detector, or by laser noise, which depends on the power of the two beams.

In an ideal case when the system is shot-noise limited and the signal beam is from a single reflection, the conventional OCDR system SNR is

$$\left(\frac{S}{N}\right)_{\text{conv}} = \frac{2P_{\text{r}}P_{\text{s}}}{P_{\text{r}} + P_{\text{s}}}\frac{\eta_d}{h\nu B}, \tag{24}$$

where η_d is the photodetector quantum efficiency, $P_{r,s}$ are the total powers of the reference and signal beams, and B

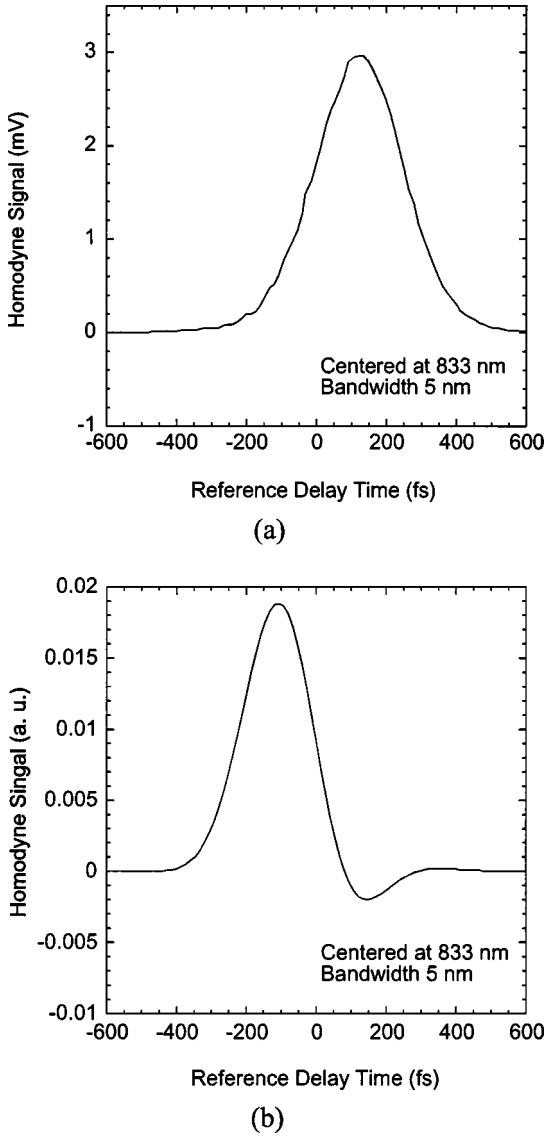

Fig. 8. Adaptive OCDR delay scan trace by broadband homodyne detection: (a) Experimental results with 5-nm-bandwidth laser pulses centered at 833 nm. (b) Simulations for the same conditions.

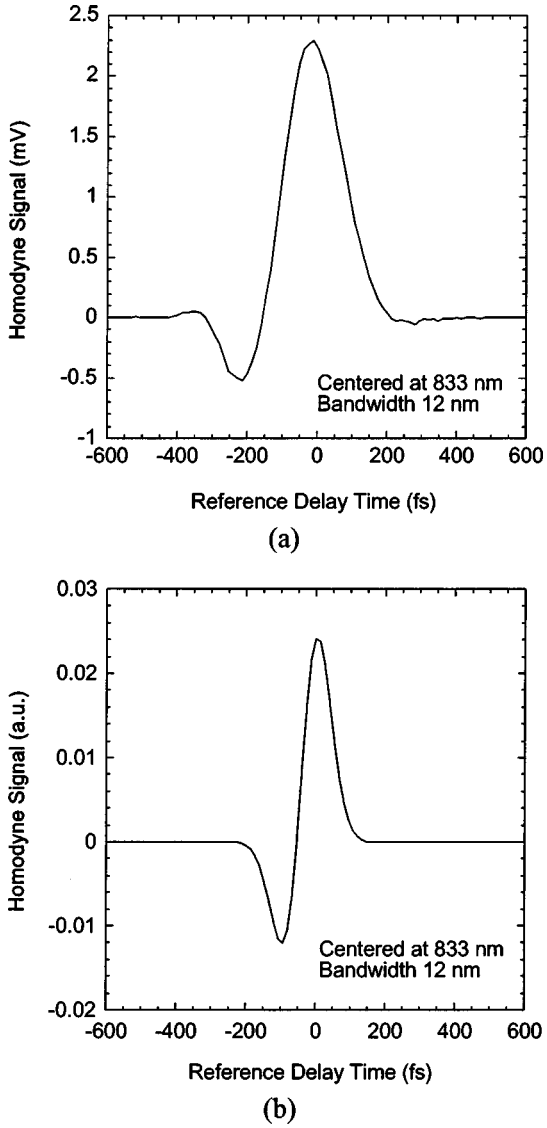

Fig. 9. Adaptive OCDR delay scan traces by broadband homodyne detection: (a) Experimental result with 12-nm-bandwidth laser pulses centered at 833 nm. (b) Simulation under nominally the same conditions, but assuming transform-limited pulses.

is the electronic detection bandwidth. Compared with conventional OCDR, the SNR of adaptive OCDR is

$$\frac{S}{N} = \exp(-\alpha L)\frac{4P_r}{P_r + P_s}\eta(\omega)[J_0(\Delta_\phi)\sin(\Delta_\phi)]^2\left(\frac{S}{N}\right)_{\text{conv}}. \tag{25}$$

The extra term in Eq. (25) represents the loss due to the adaptive holographic beam combining. This includes (1) the absorption of the PRQW device, which has an average absorption coefficient of $5 \times 10^3\ \text{cm}^{-1}$ over an approximately 1-μm-thick film, (2) the fringe wash-out by fast phase modulation, and (3) a limited diffraction efficiency $\eta(\omega)$ of $\sim 0.5\%$. In the shot-noise limit, these factors cost adaptive OCDR a 15-dB loss in sensitivity. In the small-signal limit, when the reference-beam intensity is much larger than the signal-beam intensity, the minimal detectable reflectance power of adaptive OCDR is 5 fW for a photodetector quantum efficiency η_d of 70% and a 30-Hz detection bandwidth achieved by a 10-ms lock-in integrating time.

Adaptive OCDR could achieve shot-noise-limited performance with a high-sensitivity detector that can sense femtowatts optical power, such as photon multiplier. But in applications, a higher-sensitivity detector is prone to be saturated by the incoherent background, which is reflections outside of the coherence gating set by the delay; as a result, to avoid detector saturation, a less sensitive but more robust detector is used. The sensitivity of the system is likely limited by the dynamic range of the photodetector. Conventional OCDR shares the similar limitation, but because the reference and signal beams are mixed on the photodetector in conventional OCDR, the main limit is the balance between the high reference power that is necessary to generate a detectable interference signal from a weak reflection and the interference signal that buries in the high-power reference. Adaptive OCDR never achieves a reference power at the detector larger than the coherent reflection power. Therefore the detector only suffers from the incoherent background in the signal beam. In applications, this advantage may compensate the theoretical 15-dB sensitivity loss.

On the other hand, adaptive OCDR has a disadvantage in the dynamic range, i.e., range between maximal and minimal detectable reflections. Homodyne powers in adaptive OCDR fall off faster with weaker coherent reflection relative to conventional OCDR. For a constant reference beam power that is much stronger than the coherence reflection, the adaptive OCDR signal follows the coherence reflection power as

$$\delta P_d \propto \exp(-\alpha L)\sqrt{\eta(\omega_0)}m\sqrt{P_r P_{\text{cor}}} \propto P_{\text{cor}}, \tag{26}$$

whereas for conventional OCDR, this is

$$(\delta P_d)_{\text{conv}} \propto \sqrt{P_r P_{\text{cor}}} \propto \sqrt{P_{\text{cor}}}. \tag{27}$$

To achieve the same reflection-power dynamic range, the adaptive approach requires a detector with a decibel dynamic range twice the decibel range that would be sufficient for conventional OCDR. This higher requirement on the detector will lead to sacrificing reflection-power dynamic range, which means losing sensitivity on weak-reflecting structures in highly heterogeneous samples.

It is interesting to make a comparison with holographic optical coherence imaging[6] (OCI), which is a full-frame imaging approach that uses PRQW devices for direct imaging inside tissue. Holographic OCI is background free in the sense that the incoherent background in the signal beam does not fall on the CCD detector, which preserves the full dynamic range of the detector for the coherent information. In the small-signal limit, the imaging intensity of holographic OCI is

$$P_d \propto \exp(-\alpha L)\eta(\omega_0)m^2 P_r \propto P_s, \tag{28}$$

which follows the same power dependence with adaptive OCDR signals but at a lower power level. The minimal detectable reflection power of holographic OCI is higher than adaptive OCDR if both are shot-noise limited, but because it is incoherent background free, it is more practical for highly scattering structures.

The sensitivity of our system was tested experimentally by penetrating a highly scattering turbid medium. Figure 10 shows adaptive homodyne traces with increasing turbid-medium thickness taken with 12-nm-bandwidth laser pulses. Pulse characterization results of the 12-nm pulse are shown in Fig. 3(b); 12-nm pulses instead of 5-nm transform-limited pulses were used in the laser ranging experiment for better depth resolution. With 12-nm-bandwidth laser pulses, the cross-correlation peak is 185 fs wide at half-maximum. The width of the homodyne traces is 185 fs, equivalent to a 28-μm depth resolution in reflectometry, which matches the electric field autocorrelation results of the laser pulse shown in Fig. 3(b). The signal-beam size at the PRQW device was approximately 1 mm in diameter, and the reference beam size is approximately 1.5 mm in diameter. We started with a clear medium with a total light intensity at 100 mW/cm^2 and β, the beam-intensity ratio of the reference beam to the signal beam at the PRQW device, equal to 3. We maintained β by decreasing the reference intensity while increasing the optical thickness of the turbid medium. By the time the optical thickness approached 13 MFP, with 3 μW of reference power at the PRQW device, the system noise was dominated by electronic noise. Thereafter, the reference-beam power at the PRQW device was kept constant at 3 μW. As shown in Fig. 10, with 200-μW incident power on the turbid media, the system detects reflections that have been attenuated by turbid media with total travel path lengths from 0 to 9.8 mean free path (MFP), and with 200-mW incident power, the path length increased to 16.4 MFP (which corresponds to 1 mm deep into human skin). The photodetector used in our experiment has a sensitivity limit of 1 nW. In both cases, the system reaches its penetration limits when the signal-beam power on the detector dropped to its sensitivity limit.

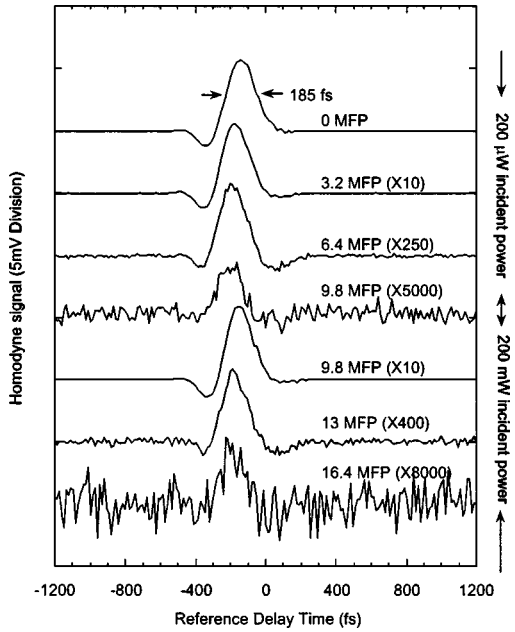

Fig. 10. Adaptive OCDR traces of a single reflection behind a turbid medium with total travel lengths from 0 to 16.4 MFPs (redrawn from Ref. 27). Data for 0–9.8 MFPs were measured with 200-μW incident power, and for 9.8–16.4 MFPs were measured with 200-mW incident power.

Compared with conventional OCDR, adaptive approaches are not superior in sensitivity, mostly because of the low diffraction efficiency of PRQW devices. There are photorefractive materials[20] with higher diffraction efficiency, which would bring the sensitivity close to conventional OCDR, but the response rates are typically slower than PRQW devices and may not be enough for high-speed acquisition. The adaptive losses must be evaluated against the gain in real applications, and the choice of adaptive material, environment, and optical characters of the sample all play roles in such an evaluation.

7. ADAPTIVE ULTRASOUND DETECTION THROUGH TURBID MEDIUM

An OCDR system based on adaptive interferometry can also be combined with laser-based ultrasound (LBU). Ultrasound imaging provides reasonable contrast for detecting internal physiological structure and has moderate spatial resolution (approximately millimeter).[21] Higher resolution is possible by incorporating optical techniques into ultrasonic imaging because of the short optical wavelengths. Optical detection modalities have been developed to image into tissue using photon diffusion either by all-optical modulation with spatial resolution limited to several millimeters[22] or by "tagging" the light with focused ultrasound that can penetrate tissue readily and can be focused to spot sizes of a millimeter.[23–25] The combination of OCDR and LBU differs from optoacoustic techniques by detecting the ultrasound at localized points inside a sample or beyond an obstacle rather than at the medium surface, and it differs from the acousto-optic tagged photon diffusion techniques by the high spatial resolution of coherence-domain techniques. LBU would normally require the condition of phase quadrature (π/2 relative phase between the signal and reference) to be maintained to yield maximum linear detection of small-signal phase modulation. But the combination is possible with adaptive interferometry that self-compensates changing spatial and temporal phase between the reference and the phase-modulated signal and maintains the phase-quadrature condition.

Laser-based ultrasound detection detects a small phase modulation from acoustic displacements. The phase-quadrature condition is necessary in ultrasound detection because of the high-sensitivity requirement to detect small phase modulations. Narrow-band detection is used and the detection wavelength is carefully chosen to satisfy the quadrature condition, as in Eq. (23). The narrow-band-detected homodyne signal at the quadrature wavelength is

$$\delta P_d(\omega_q, \tau; t) = 2\exp[-\alpha(\omega_d)L] \times \langle m(\tau)\rangle \sqrt{\eta(\omega_d)}\sqrt{I_s(\omega_d)I_r(\omega_d)}\Delta\omega_d \times \sin[-(\omega_d - \omega_s)\tau + \phi(t)], \quad (29)$$

where $\Delta\omega_d$ is the optical detecting bandwidth, and the phase modulation is $\phi(t) = 4\pi/\lambda d(t)$, which is caused by ultrasonic vibrations $d(t)$. The homodyne signal is most sensitive to the surface displacement at path match

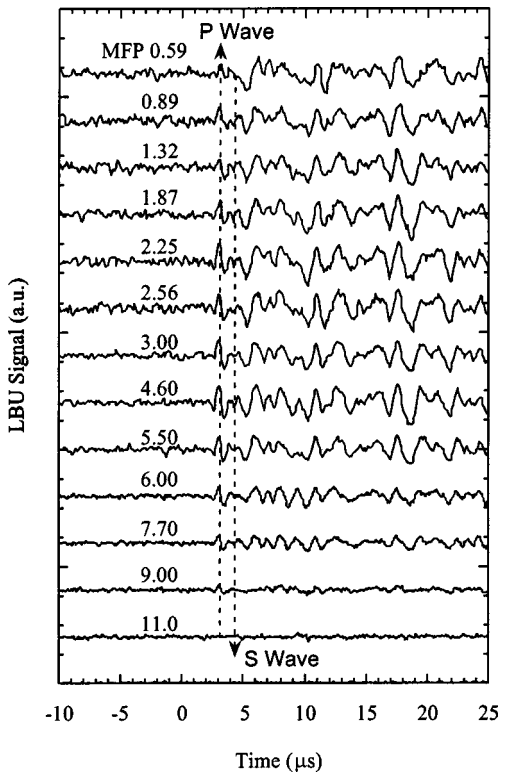

Fig. 11. Laser-based ultrasound (LBU) signal versus increasing optical thickness from 0.59 MFP to 11 MFP (redrawn from Ref. 28). The signal was detected at the quadrature wavelength with 1-nm detection bandwidth at zero relative time delay. Beam-intensity ratio β at the PRQW devices was maintained at a value of 3 by decreasing the reference intensity while increasing the optical thickness of the turbid medium.

$$\delta P_d(\omega_d, 0; t) = 2 \exp[-\alpha(\omega_d)L]\langle m(0)\rangle \sqrt{\eta(\omega_d)} \times \sqrt{I_s(\omega_d) I_r(\omega_d)}\Delta\omega_d \sin\left[\frac{4\pi}{\lambda} d(t)\right]. \tag{30}$$

The minimum detectable surface displacement is the displacement that generates a signal amplitude that is equal to the root-mean-square noise. At the shot-noise limit, the minimum detectable surface displacement would be

$$\Delta d_{\min} = \frac{\lambda}{4\pi} \frac{\exp[\alpha(\omega_d)L/2]\sqrt{h\nu B}}{2m\sqrt{\eta(\omega_d)\eta_d I_r(\omega_d)\Delta\omega_d}}. \tag{31}$$

A laser ultrasound receiver sensitivity can be quantified as a noise-equivalent surface displacement, corresponding to the minimum detectable displacement with 1-mW incident power and 1-Hz electronic bandwidth. It has been proved that shot-noise-limited adaptive LBU is sensitive to subpicometer surface displacements.[26] In adaptive OCDR-based ultrasound detection experiment, the penetration ability of OCDR is combined with the high surface displacement sensitivity by using the broadband light source. The noise-equivalent surface displacement of the system is

$$\Delta d_{\min} = \frac{\lambda}{4\pi} \frac{\exp[\alpha(\omega_q, F)L/2]\sqrt{h\nu}}{2m\sqrt{\eta(\omega_q)\eta_d}} \times \frac{1}{\sqrt{\eta_{\Delta\omega}}}, \tag{32}$$

where $\eta_{\Delta\omega}$ is energy efficiency of narrow-band detection on the broadband spectrum. The last factor in Eq. (32) represents the sensitivity loss compared with cw adaptive LBU,[26] coming from the light energy loss in narrow-band detection on the broadband spectrum. For a 13-nm Gaussian spectrum, the energy efficiency of 1-nm narrow-band detection at the peak is 7%; thus the noise-equivalent surface displacement is larger by a factor of 4 when adaptive LBU is combined with OCDR.

Figure 11 shows laser-based ultrasound signals under different turbid optical thicknesses detected at the quadrature wavelength with 1-nm bandwidth at zero relative time delay. The temporal responses of the homodyne signals were detected by a high-speed APD (Hamamatsu, C5658), amplified by an ultrasonic preamplifier (Panametrics, 5660B), bandpass filtered at 2 MHz with 3.5-MHz bandwidth, and then acquired by a digital oscilloscope with a 20-MHz bandwidth in an acquisition mode with an average of 100 waveforms. The signal traces show vibrations at a megahertz frequency. Wave fronts of the compression waves (P wave) and shear waves (S wave) can be recognized. A rapid signal drop was experienced beyond an optical thickness of 4 MFP, while the trace shape was well preserved despite the increasing penetration depth. The homodyne signal was detected even when the signal beam passed through the turbid media with an optical thickness of 11 MFP.

8. CONCLUSION

In conclusion, we have described the use of an adaptive interferometer to perform optical coherence-domain reflectometry. Optimal modulation and depth resolution of adaptive OCDR have been discussed, as well as the time-spectral two-dimensional homodyne readout process. Experiments proved the first system has 16-MFP travel depth and can be combined with ultrasound detection beneath turbid media. Certain limitations such as sensitivity and dynamic range do exist, but these limitations are paid for by a lot of advantages: By combining the waves adaptively, mechanical vibration and multimode speckle are removed in the coherent detection signal. For homodyne-detection applications, the adaptive interferometer provides stability. The quadrature condition is maintained independently of drifting optical components, which creates the ability of combining ultrasound detection with delay line scan. The full speckle field can be captured because each speckle is phase locked, and all work in unison to provide strong signal modulation, which improves detection efficiency.

However, it must be pointed out that an application such as rapid-scan OCT, which relies on heterodyne detection, would not likely benefit from the adaptive approach because the sweeping phase of the detected signal requires no phase locking, and single-mode illumination (as from a confocal microscope or a single-mode fiber) would not need the speckle-compensation capabilities. Nonetheless, other applications such as *en face* scanning that works at fixed delay, or full-field imaging,[6] could benefit from the adaptive approach explored here.

This work was support by the National Center for Research Resources of the National Institutes of Health under grant R21 RR15040-02 and by the National Science Foundation under grant ECS-0200424.

REFERENCES

1. E. A. Swanson, D. Huang, M. R. Hee, J. G. Fujimoto, C. P. Lin, and C. A. Puliafito, "High-speed optical coherence domain reflectometry," Opt. Lett. **17**, 151–153 (1992).
2. R. C. Youngquist, S. Carr, and D. E. N. Davies, "Optical coherence-domain reflectometry: a new optical evaluation technique," Opt. Lett. **12**, 158–160 (1987).
3. D. Huang, E. A. Swanson, C. P. Lin, J. S. Schuman, W. G. Stinson, W. Chang, M. R. Hee, T. Flotte, K. Gregory, C. A. Puliafito, and J. G. Fujimoto, "Optical coherence tomography," Science **254**, 1178–1181 (1991).
4. J. A. Rogers, A. G. Podoleanu, G. Dobre, D. A. Jackson, and F. W. Fitzke, "Topography and volume measurements of the optics nerve using *en-face* optical coherence tomography," Opt. Express **9**, 533–545 (2001).
5. J. M. Schmitt, S. H. Xiang, and K. M. Yung, "Speckle in optical coherence tomography," J. Biomed. Opt. **4**, 95–105 (1999).
6. P. Yu, M. Mustata, J. J. Turek, P. M. W. Frech, M. R. Melloch, and D. D. Nolte, "Holographic optical coherence imaging of tumor spheroids," Appl. Phys. Lett. **83**, 575–577 (2003).
7. D. D. Nolte, "Semi-insulating semiconductor heterostructures: optoelectronic properties and applications," J. Appl. Phys. **85**, 6259–6289 (1999).
8. Y. Ding, I. Lahiri, D. D. Nolte, G. J. Dunning, and D. M. Pepper, "Electric-field correlation of femtosecond pulses by use of a photoelectromotive-force detector," J. Opt. Soc. Am. B **15**, 2013–2017 (1998).
9. S. Stepanov, P. R. Montero, M. A. C. Flores, J. C. Mixcoatl, A. A. López, L. A. Carrasco, and M. S. Sánchez, "Interferometric applications of GaAs adaptive photo-EMF detectors," J. Opt. Technol. **69**, 428–431 (2002).
10. F. M. Davidson and L. Boutsikaris, "Homodyne detection using photorefractive materials as beamsplitters," Opt. Eng. **29**, 369–377 (1990).
11. J. Khoury, V. Ryan, C. Woods, and M. Cronin-Golomb, "Photorefractive optical lock-in detector," Opt. Lett. **16**, 1442–1444 (1991).
12. R. K. Ing and J.-P. Monchalin, "Broadband optical detection of ultrasound by two-wave mixing in a photorefractive crystal," Appl. Phys. Lett. **59**, 3233–3235 (1991).
13. I. Rossomakhin and S. I. Stepanov, "Linear adaptive interferometers via diffusion recording in cubic photorefractive crystals," Opt. Commun. **86**, 199–204 (1991).
14. D. D. Nolte, T. Cubel, L. J. Pyrak-Nolte, and M. R. Melloch, "Adaptive beam combining and interferometry using photorefractive quantum wells," J. Opt. Soc. Am. B **18**, 195–205 (2001).
15. S. Balasubramanian, I. Lahiri, Y. Ding, M. R. Melloch, and D. D. Nolte, "Two-wave mixing dynamics and nonlinear hot-electron transport in transverse-geometry photorefractive quantum wells studied by moving gratings," Appl. Phys. B **68**, 863–869 (1999).
16. R. M. Brubaker, Q. N. Wang, and D. D. Nolte, "Nonlocal photorefractive screening from hot electron velocity saturation on semiconductors," Phys. Rev. Lett. **77**, 4249–4252 (1996).
17. R. M. Brubaker, Q. N. Wang, D. D. Nolte, E. S. Harmon, and M. R. Melloch, "Steady-state four-wave mixing in photorefractive quantum wells with femtosecond pulses," J. Opt. Soc. Am. B **11**, 1038–1044 (1994).
18. L. Lepetit, G. Cheriaux, and M. Joffre, "Linear techiques of phase measurement by femtosecond spectral interferometry for applications in spectroscopy," J. Opt. Soc. Am. B **12**, 2467 (1995).
19. R. Jones, D. D. Nolte, and M. R. Melloch, "Adaptive femtosecond optical pulse combining," Appl. Phys. Lett. **77**, 3692–3694 (2000).
20. D. D. Nolte, ed., *Photorefractive Effects and Materials*, Electronic Materials: Science and Technology Series (Kluwer Academic, Dordrecht, The Netherlands, 1995).
21. S. Webb, *The Physics of Medical Imaging* (Institute of Physics, University of Reading, Berkshine, UK, 1988).
22. B. Chance, K. Kang, L. He, J. Weng, and E. Sevick, "Highly sensitive object location on tissue models with linear in-phase and anti-phase multi-element optical arrays in one and two dimensions," Proc. Natl. Acad. Sci. (USA) **90**, 3423 (1993).
23. A. Lev, Z. Kolter, and B. G. Sfez, "Ultrasound tagged light imaging in turbid media in a reflectance geometry," Opt. Lett. **25**, 378–380 (2000).
24. M. Hisaka, T. Sugiura, and S. Kawata, "Optical cross-sectional imaging with pulse ultrasound wave assistance," J. Opt. Soc. Am. A **18**, 1531–1534 (2001).
25. L. Wang and X. Zhao, "Ultrasound-modulated optical tomography of absorbing objects buries in dense tissue-simulating turbid media," Appl. Opt. **36**, 7727–7782 (1997).
26. I. Lahiri, L. J. Pyrak-Nolte, D. D. Nolte, M. R. Melloch, R. A. Kruger, G. D. Bacher, and M. B. Klein, "Laser-based ultrasound detection using photorefractive quantum wells," Appl. Phys. Lett. **73**, 1041–1043 (1998).
27. L. Peng, P. Yu, D. D. Nolte, and M. R. Melloch, "High-speed adaptive interferometer for optical coherence-domain reflectometry through turbid media," Opt. Lett. **26**, 396–398 (2003).
28. P. Yu, L. Peng, D. D. Nolte, and M. R. Melloch, "Ultrasound detection through turbid media," Opt. Lett. **28**, 819–821 (2003).